Dosimetric impact of geometric distortions in an MRI-only proton therapy workflow for lung, liver and pancreas

Hatice Selcen Dumlu[1,2], **Giorgia Meschini**[1], **Christopher Kurz**[3], **Florian Kamp**[3], **Guido Baroni**[1,4], **Claus Belka**[3,5], **Chiara Paganelli**[1], **Marco Riboldi**[2,*]

[1] Department of Electronics, Information and Bioengineering, Politecnico di Milano, Via Ponzio 34/5, 20133 Milano, Italy
[2] Department of Medical Physics, Faculty of Physics, Ludwig-Maximilians-Universität München, Am Coulombwall 1, 85748 Garching bei München, Germany
[3] Department of Radiation Oncology, University Hospital, LMU Munich, Marchioninistraße 15, 81377 München, Germany
[4] Centro Nazionale di Adroterapia Oncologica, Strada Campeggi 53, 27100 Pavia, Italy
[5] German Cancer Consortium (DKTK) partner site Munich, Germany and German Cancer Research Center (DKFZ), Im Neuenheimer Feld 280, 69120 Heidelberg, Germany

Received 27 February 2020; accepted 1 October 2020

Abstract

In a radiation therapy workflow based on Magnetic Resonance Imaging (MRI), dosimetric errors may arise due to geometric distortions introduced by MRI. The aim of this study was to quantify the dosimetric effect of system-dependent geometric distortions in an MRI-only workflow for proton therapy applied at extra-cranial sites. An approach was developed, in which computed tomography (CT) images were distorted using an MRI displacement map, which represented the MR distortions in a spoiled gradient-echo sequence due to gradient nonlinearities and static magnetic field inhomogeneities.

A retrospective study was conducted on 4DCT/MRI digital phantoms and 18 4DCT clinical datasets of the thoraco-abdominal site. The treatment plans were designed and separately optimized for each beam in a beam specific Planning Target Volume on the distorted CT, and the final dose distribution was obtained as the average. The dose was then recalculated in undistorted CT using the same beam geometry and beam weights. The analysis was performed in terms of Dose Volume Histogram (DVH) parameters.

No clinically relevant dosimetric impact was observed on organs at risk, whereas in the target structure, geometric distortions caused statistically significant variations in the planned dose DVH parameters and dose homogeneity index (DHI). The dosimetric variations in the target structure were smaller in abdominal cases ($\Delta D_{2\%}$, $\Delta D_{98\%}$, and ΔD_{mean} all below 0.1% and ΔDHI below 0.003) compared to the lung cases. Indeed, lung patients with tumors isolated inside lung parenchyma exhibited higher dosimetric variations ($\Delta D_{2\%} \geq 0.3\%$, $\Delta D_{98\%} \geq 15.9\%$, $\Delta D_{mean} \geq 3.3\%$ and $\Delta DHI \geq 0.102$) than lung patients with tumor close to soft tissue ($\Delta D_{2\%} \leq 0.4\%$, $\Delta D_{98\%} \leq 5.6\%$, $\Delta D_{mean} \leq 0.9\%$ and $\Delta DHI \leq 0.027$) potentially due to higher density variations along the beam path. Results suggest the potential applicability of MRI-only proton therapy, provided that specific analysis is applied for isolated lung tumors.

Keywords: MRI-only radiotherapy, Proton therapy, MR geometric distortion, Thoraco-abdominal cancer

* Corresponding author: Marco Riboldi, Chair of Experimental Physics – Medical Physics, Faculty of Physics, Ludwig-Maximilians-Universität München, Am Coulombwall 1, 85748 Garching bei München, Germany.
E-mail: marco.riboldi@physik.uni-muenchen.de (M. Riboldi).

Z Med Phys **32** (2022) 85–97
https://doi.org/10.1016/j.zemedi.2020.10.002
www.elsevier.com/locate/zemedi

1 Introduction

Thanks to the favorable physical properties of protons, external beam proton therapy entails several clinical advantages, by allowing for a highly conformal dose to the target volume at a reduced integral dose and greater sparing of normal tissues in comparison to conventional photon therapy [1–3].

Medical imaging plays an important role in the treatment planning of state-of-the-art radiotherapy techniques [4], with Computed Tomography (CT) being the current clinical standard. CT provides (i) a geometrically accurate representation of the patient anatomo-pathological configuration and (ii) information on electron density in the case of photon therapy. In proton therapy, CT Hounsfield Units (HU) are converted into stopping power ratio relative to water, which is necessary for dose calculation [5]. As a complementary imaging modality, Magnetic Resonance Imaging (MRI) has been also adopted, since it contributes significantly to the target delineation with its superior soft tissue contrast compared to CT [6,7]. Conventional treatment planning in modern radiation therapy procedures is based on the hybrid workflow of CT and MRI, in which image registration is performed to define a spatial relationship between the two images [7,8]. However, with this approach, systematic spatial uncertainties are introduced as a result of the multimodal image registration and inter-scanner differences can potentially occur between the two imaging sessions [8–11]. Moreover, the increased cost when using two imaging modalities and patient exposure to ionizing radiation in the CT acquisition are also undesirable [7,12].

Due to the limitations of CT/MRI hybrid workflows [13,14], techniques excluding CT are under investigation. These workflows are referred to as 'MRI-only' – also as 'MRI-based' or 'MRI-alone' – radiation therapy, where a synthetic CT is generated from MRI to replace CT and enable dose calculation [14–16]. Several techniques have been introduced for synthetic CT generation [17–20], aiming at radiation-free treatment planning and reduced time, effort, and resources.

Despite these advantages, the use of MRI in treatment planning raises challenges, since MR images can suffer from geometric distortions [21–24]. Geometric distortions can be categorized as system- and patient-dependent distortions [21,25]. The system-dependent distortions are mainly caused by nonlinearities of the gradient field and inhomogeneities in the main static magnetic field (B_0) [26], increasing with the distance from the MRI system isocenter [27]. Patient-dependent distortions are related to the magnetic properties of the patient under scan and mainly stem from magnetic susceptibility and chemical shift effects [23]. System-dependent distortions are larger than patient-dependent distortions in magnitude, but they would be ideally reduced in modern MR scanners [28,29].

For the measurement and mapping of MRI distortions, phantom-based techniques are the most commonly used approaches [30–32]: the discrepancy in the positions of markers in the phantom between the CT images (i.e., gold standard) and the MR images is typically measured to characterize MRI distortions. Vendor-supplied distortion correction algorithms and magnetic field shimming can be used to partially correct for MRI distortions, though geometric inaccuracies still remain [25,28].

Such inaccuracies may result in dosimetric uncertainties, with subsequent insufficient irradiation of the tumor and over-dosage in surrounding healthy tissues [34–36]. Thus, a thorough investigation of the dosimetric impact of the geometric distortions in an MRI-only workflow has to be established for the clinical introduction of MRI-only radiotherapy. Up to the current knowledge, all of the studies in the literature on the investigation of the effect of system- and patient-dependent image distortions on the radiation dose in the MRI-only workflow are made in conventional photon radiation therapy [33–35], with no known study in proton therapy. Indeed, the effect has not been systematically studied for lung, liver and pancreas, where respiration-induced tumor motion is a major obstacle for high precision irradiation. In the lung, liver, and pancreas, proton therapy has shown promising results in terms of local control, survival and minimization of dose to OARs [36,37], provided that organ motion and variation in the patient anatomy along the beam path are properly accounted for, as they can result in severe degradation of the delivered dose [38]. In line with this, it is extremely important to investigate the dosimetric impact of geometric distortions in MRI-only proton therapy for thoraco-abdominal sites where respiratory motion-compensated irradiation is essential for dosimetric accuracy. In the case of MRI-only proton therapy, literature studies mostly focused on the dosimetric effects of errors originating from synthetic CT generation methods [39–47], neglecting the MR geometric distortions.

The aim of this work is to quantify the dosimetric effect of system-dependent geometric distortions in an MRI-only proton therapy workflow of the thoraco-abdominal site. The specific goal is to verify whether accurate proton treatment planning is able to account for such effects, resulting in acceptable dosimetric results. The developed methodology enables us to account for dosimetric changes purely due to geometric distortions, eliminating the inaccuracies arising from synthetic CT generation techniques. Specifically, 4D CT scans of lung, liver, and pancreas are used in combination with displacement maps of geometric distortions to evaluate geometric and especially dosimetric changes.

2 Materials and methods

2.1 Imaging dataset

Treatment plan simulations were first performed on a digital breathing thoraco-abdominal phantom to provide a reference

with a realistic human model, in comparison to clinical data. The 4D CT/MRI Breathing Anthropomorphic Thorax (CoMBAT) phantom developed by Paganelli et al. [48] was used in this study. The phantom dataset comprised two lung phantoms, with the tumors (tumor size 2.01 cm^3) at different locations inside the lung parenchyma, a liver phantom (tumor size 13.83 cm^3), and a pancreas phantom (tumor size 13.83 cm^3).

Treatment plan simulations were also performed on clinical 4D CT datasets including 10 patients with lung cancer (2 female and 8 male, age range: 58–82), 4 patients with liver (3 female and 1 male, age range: 35–78), and 4 patients with pancreas cancer (2 female and 2 male, age range: 69–84). Patients have been treated with intensity modulated photon radiotherapy and retrospectively analyzed. Baseline patient characteristics are summarized in Table 1. Patient CT images were acquired using a Toshiba Aquilion LB CT scanner (Canon Medical Systems Cooperation, Japan) with 550 mm × 550 mm field-of-view, in-plane resolution of 1.074 × 1.074 mm^2, slice thickness of 3 mm in lung image acquisitions and 2 mm in liver and pancreas image acquisitions. The tube voltage was set to 120 kV, with exposure time of 500 ms, and tube current of 150 mA. Abdominal compression was applied during the acquisition of patients with liver cancer in order to reduce the peak-to-peak motion amplitude.

Each phantom and patient dataset used in this study included CT images of 10 respiratory phases and an average CT. The gross tumor volume (GTV) in each respiratory phase and Organs at Risk (OARs) in the average CT were manually contoured in case of phantoms data on the open-source software environment CERR (Computational Environment for Radiological Research) [49], whereas they were contoured by expert radiation oncologists in the case of clinical data. All data were resampled to the same voxel size (1.074 × 1.074 × 3 mm^3), in agreement with clinical data settings.

2.2 Displacement map generation

Residual geometric distortion quantification was obtained for a Magnetom AERA 1.5 T Scanner from Siemens. A displacement map, represented as Deformation Vector Field (DVF), was generated by experimental quantification of the system-dependent geometric distortions using a self-designed distortion phantom. The displacement map calculated for a spoiled gradient-echo sequence (sGRE) was used, relying on axial image stacking (5 mm thickness) and 3D distortion correction. The utilized sGRE sequence featured the following characteristics: echo time 2.78 ms, repetition time 5.80 ms, flipping angle 8°, bandwidth per pixel 295 Hz, voxel size 1.172 × 1.172 × 5 mm^3. The demonstrated geometric distortion in the sGRE sequence had a mean in-slice landmark deformation up to 1 mm and maximal mean landmark deformation up to 3 mm in the slice selection direction at 105 mm distance from the MRI system isocenter. Deformations were strongly dependent on the position within the field of view, with a rather symmetric behavior around the imaging isocenter (Figure A.1). As such, the average (absolute max) of observed 3D geometric distortions using the self-designed phantom were 0.0 mm (11.6 mm), −0.2 mm (13.5 mm), and 0.0 mm (4.3 mm) in the *X*, *Y* and *Z* directions, respectively. The details of the approach for the assessment and representation of geometric distortions in MRI are provided in Appendix A and described in detail by Kroll et al [50].

2.3 Treatment planning

The pencil-beam scanning proton treatment plan simulations were performed in the in-house particle therapy extension of the CERR treatment planning system [49,51]. The treatment plan workflow used in this study is summarized with a flow chart in Figure 1.

In order to model respiratory motion-compensated irradiation, a gated treatment was simulated at the exhale phase, as implemented clinically in proton therapy facilities [52]. Accordingly, 3 GTVs around end-exhale were combined to form the internal target volume (ITV). As reported in Kang et al. (lung case), Hong et al. (liver case), and Jethwa et al. (pancreas case), the clinical target volume (CTV) was defined by 8 mm isotropic expansion of the ITV [53–55]. Considering that simple isotropic expansion of CTV volumes to create the planning target volume (PTV) is inadequate in proton therapy treatment planning [56,57], a beam specific PTV (bsPTV), which takes into account set-up error and systematic range uncertainties, was generated following the approaches by Moyers et al. [56] and Paganetti [3].

The proton treatment fields were designed to best conform the dose to the CTV with the prescribed dose of 2 GyE/fraction in the lung and liver cases and 3 GyE/fraction in the pancreas cases. The treatment plan optimizations were performed on the average CT volume. The proton treatment fields consisted of two beams, and gantry angles were determined case by case. In the lung cases, the beams allowing the shortest possible distance to the tumor and avoiding a beam path through the contralateral lung and the heart were selected. For the liver cases, the two beams were arranged in the lateral (range of 275°–280°) and anterior directions (range of 0°–10°) and, for the pancreas cases, two oblique fields (ranges of 120°–150° and 200°–240°) were used. After determining the optimal beam angles, bsPTVs were generated for each field in Raystation (Raysearch Laboratories, Stockholm, Sweden) using the structure definition with beam specific margin functionality. Beam specific distal and proximal margins were calculated assuming a proton range uncertainty of 3.5% of the range plus an additional 3 mm [56], based on the most distal and proximal water-equivalent depth of the CTV contour on the beam path, respectively. Then, a 3 mm lateral margin in the beam's eye view was added to account for set-up errors.

In order to spare the healthy tissues nearby the tumor volume, a ring concentric to the bsPTV was generated by an

Table 1
Patient and treatment characteristics. The tumor size was computed across the 10 4D CT phases.

Anatomical Site	Patient no	Tumor size (mean±STD) [cm^3]	CC motion [cm]	A-P motion [cm]	L-R motion [cm]
Lung	Patient 1	0.9±0.1	0.6	0.4	0.3
	Patient 2	5.9±0.2	0.9	0.2	0.2
	Patient 3	14.6±1.5	0.9	0.5	0.3
	Patient 4	16.2±0.4	0.9	0.3	0.2
	Patient 5	1.4±0.1	1.2	0.3	0.2
	Patient 6	2.9±0.1	0.9	0.8	0.3
	Patient 7	12.6±0.9	1.5	0.3	0.1
	Patient 8	4.4±0.4	1.2	1.0	0.3
	Patient 9	5.3±0.8	0.9	0.3	0.1
	Patient 10	3.6±0.5	0.9	0.5	0.3
Liver	Patient 1	20.1±4.0	1.0	0.2	0.3
	Patient 2	20.2±1.2	1.0	0.3	0.3
	Patient 3	0.7±0.3	2.1	0.5	0.3
	Patient 4	4.9±0.3	0.6	0.3	0.3
Pancreas	Patient 1	64.1±5.3	0.6	0.3	0.3
	Patient 2	0.7±0.1	0.8	0.2	0.2
	Patient 3	39.5±2.6	1.0	0.4	0.2
	Patient 4	6.4±0.5	0.8	0.3	0.20

Abbreviations: CC, Cranial Caudal; A-P, Anterior Posterior; L-R: Left Right.

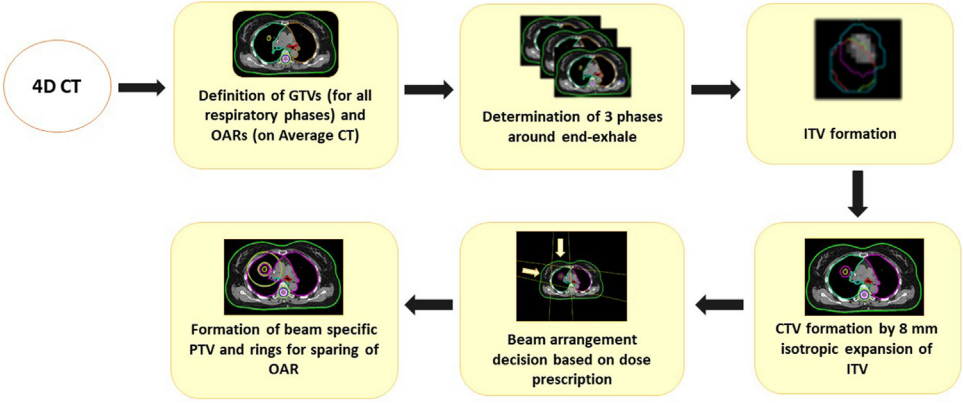

Figure 1. Treatment planning workflow used in this study. GTV: Gross Tumor Volume, ITV: Internal Target Volume, PTV: Planning Target Volume, OAR: Organ at Risk, CTV: Clinical Target Volume.

isotropic expansion of the bsPTV by 3 cm to 4 cm, excluding the bsPTV inside; the single-field uniform dose treatment plans were optimized by aiming at 0 GyE dose delivery within the ring. The radius of the rings was patient-specific, depending on the location of the tumor and the OARs, so that the nearby organs were spared.

2.4 Impact of geometric distortions

To simulate the geometric distortions arising from MRI, the DVF representing the distortion model was applied to the CT images and delineated contours using the same imaging isocenter, thus creating distorted CT images. For patients, the entity of the geometric distortion was quantified in the CTV and in the whole volume. Additionally, the mean absolute error (MAE) between the undistorted and the distorted images in the CTV and the whole body volume was computed, in order to quantify the voxel-wise intensity changes as a result of the geometric distortion application. Specifically, the MAE describing the absolute voxel-wise difference in HU was defined as:

$$\mathrm{MAE} = \frac{1}{N}\sum_{N}^{i=1} \left| Vol_{undistorted_i} - Vol_{distorted_i} \right| \quad (1)$$

where N is the number of voxels, $\mathrm{Vol}_{\mathrm{undistorted}}$ is the undistorted structure volume and $\mathrm{Vol}_{\mathrm{distorted}}$ is the distorted structure volume [15]. In case of the body volume, the union

area of the undeformed and deformed body volume masks was used to compute MAE results.

2.5 Quantification of dosimetric impact of geometric distortions

Using a pencil beam dose calculation algorithm, the treatment plan was optimized for each single field on the distorted CTs. In order to keep consistency with the MRI-only workflow in the clinical practice, the distorted dose was calculated with distorted contours where the distorted bsPTV was defined as the target. The final dose distribution for the distorted CT, denoted as $D_{distorted}$, was found as the average of the dose distributions generated from each single uniform field optimization. In the treatment plans, the treatment isocenter was defined as the isocenter of the bsPTV. Thus, the treatment isocenter was shifted in the distorted CT treatment simulations. The dose was then recalculated in the undistorted CT for each field using the same beam geometry, dose prescriptions, and the same beam weights, which were calculated in the single field optimization in the distorted CT. The final dose distribution for the undistorted CT, denoted as $D_{undistorted}$, was found following the same approach in calculating $D_{distorted}$. The workflow of the developed methodology is shown in Figure 2. $D_{undistorted}$ and $D_{distorted}$, computed on the average CT volumes, were analyzed in undistorted and distorted contour sets, respectively, and compared based on their dose–volume histogram (DVH) parameters, using the following metrics in the CTV: near-minimum dose ($D_{98\%}$), near-maximum dose ($D_{2\%}$) and mean dose (D_{mean}). The results were expressed as the percentage dose difference (normalized to the prescribed dose) between $D_{undistorted}$ and $D_{distorted}$ ($\Delta D_{98\%}$, $\Delta D_{2\%}$, ΔD_{mean}). In addition, change in the uniformity of the dose distribution in the target structure due to geometric distortions was assessed by computing the variation in dose homogeneity index (ΔDHI), where DHI was defined as:

$$DHI = \frac{D_{5\%}}{D_{95\%}} \tag{2}$$

with $D_{5\%}$ and $D_{95\%}$ being the minimum dose in the 5% and 95% volume of the CTV, respectively [58]. For the assessment of the dosimetric impact of geometric distortion in the OARs, the difference in mean dose (ΔD_{mean}) and maximum dose (ΔD_{max}) parameters between $D_{undistorted}$ and $D_{distorted}$ were calculated and normalized to $D_{distorted}$. The considered OARs were as follows:

- lung cases – spinal cord, heart, esophagus, contrary lung, and ipsilateral lung;
- liver cases – liver, right kidney, spinal cord, stomach, and large intestine;
- pancreas cases – spinal cord, liver, stomach, large intestine, and left and right kidneys.

In order to evaluate the significance of the dosimetric variations in the DVH parameters due to geometric distortions, the Wilcoxon matched-pairs signed-rank test was performed on the clinical dataset on the paired undistorted and distorted dosimetric results at the CTV structure and OARs. The ρ-value was returned for the paired, two-sided test at a 5% significance level for the null hypothesis that the absolute difference of undistorted and distorted dosimetric result pairs comes from a distribution with zero median. Then, the Kruskal–Wallis test was performed on the $\Delta D_{98\%}$, $\Delta D_{2\%}$, ΔD_{mean}, and ΔDHI metrics at the same significance level to evaluate the distribution of these parameters among different anatomical regions with the null hypothesis that the dosimetric results at each anatomical region come from the same distribution.

3 Results

3.1 Results in phantom cases

3.1.1 Impact of geometric distortions

MAEs between the undistorted CT and the distorted CT in the whole body volume were 33.14 HU, 33.89 HU, and 33.89 HU for the lung, liver, and pancreas phantoms, respectively. The MAEs in the CTV volume were 28.39 HU, 2.41 HU, and 3.82 HU for the corresponding phantoms.

3.1.2 Dosimetric impact of geometric distortions

Treatment plans on three phantom cases (lung, liver, and pancreas) are displayed in Figure 3.

Table 2 reports the dosimetric variations due to geometric distortions in the CTV DVH parameters for the phantom cases.

The differences between the undistorted and distorted dose distributions were smaller in the abdominal regions, with ΔDHI reaching a maximum value of 0.001 and the rest of the DVH parameters exhibiting a maximum dosimetric variation of 0.13% with respect to the prescribed dose. The dosimetric changes due to geometric distortions were higher in the lung region. Indeed, for the lung phantom with an isolated tumor inside the lung parenchyma, the results showed a higher difference compared to other phantoms, with ΔDHI reaching 0.048 and the dosimetric variation in terms of rest of the DVH parameters ranging between 0.70% and 8.70% of the prescribed dose.

ΔD_{mean} and ΔD_{max} in the OARs in phantom cases exhibited a maximum variation of 3.70% and 2.53% with respect to the dose in the distorted plans, respectively.

3.2 Results in the patient cohort

3.2.1 Impact of geometric distortions

The median and range of the mean geometric distortions presented within the CTV and whole body volumes in the lung, liver, and pancreas datasets are displayed in Table 3.

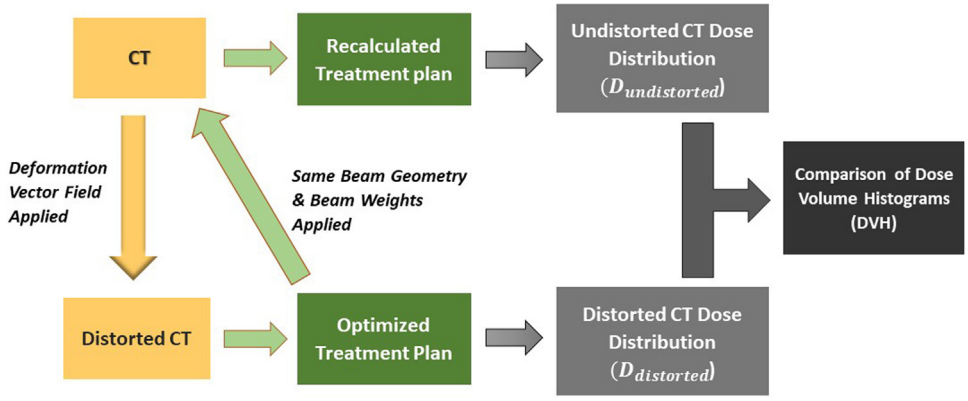

Figure 2. Flow chart of operations applied on CT image in order to quantify and analyze the dosimetric impact of geometric distortions. CT: Original CT image, $D_{undistorted}$: Dose distribution from undistorted CT, $D_{distorted}$: Dose distribution from distorted CT.

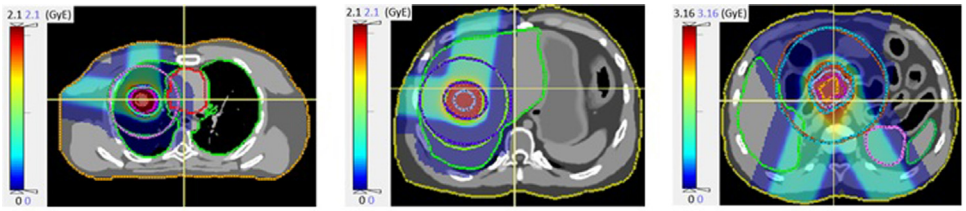

Figure 3. Phantom study: Treatment plan on the (a) lung phantom with tumor isolated inside the lung parenchyma, (b) liver phantom, (c) pancreas phantom.

Table 2
Dosimetric change in CTV DVH parameters between undistorted and distorted dose distributions in the phantom data (Dosimetric change in terms of $D_{2\%}$, $D_{98\%}$, D_{mean} DVH parameters are normalized to the prescribed dose, which was 2 GyE in lung and liver cases and 3 GyE in pancreas case).

	$\Delta D_{2\%}$ (%)	$\Delta D_{98\%}$ (%)	ΔD_{mean} (%)	ΔDHI
Lung phantom (tumor close to soft tissue)	0.40	0.40	0.25	0.007
Lung phantom (tumor isolated in lung parenchyma)	0.70	8.70	1.30	0.048
Liver phantom	0.10	0.10	0.05	0.001
Pancreas phantom	0.13	0.07	0.10	0.001

Table 3
Median and min–max range values of the geometric distortion magnitude applied within CTV and whole body volume in lung, liver and pancreas datasets.

	Geometric distortion in CTV (mm)		Geometric distortion in the whole body volume (mm)	
	Median	Range	Median	Range
Lung	2.0	0.5–3.1	2.1	0.0–12.0
Liver	2.3	0.0–3.4	2.3	0.0–13.5
Pancreas	1.4	0.4–3.2	2.2	0.0–11.8

The application of geometric distortions is demonstrated with the overlay of distorted CT on the undistorted CT in Figure 4 with an example from each studied anatomical site.

MAEs between the undistorted and distorted CT in the whole body volume had similar median values across different sites, i.e. 40.01 HU, 40.70 HU, and 39.0 HU in the lung, liver, and pancreas datasets, respectively. However, lung cases presented higher variation compared to the abdominal cases: MAEs in the whole body volume ranged from 22.55 HU to 43.88 HU, 32.90 HU to 42.71 HU, and 29.65 HU to 42.09 HU in lung, liver, and pancreas, respectively. Considering undistorted CTV vs. distorted CTV, MAEs presented lower median

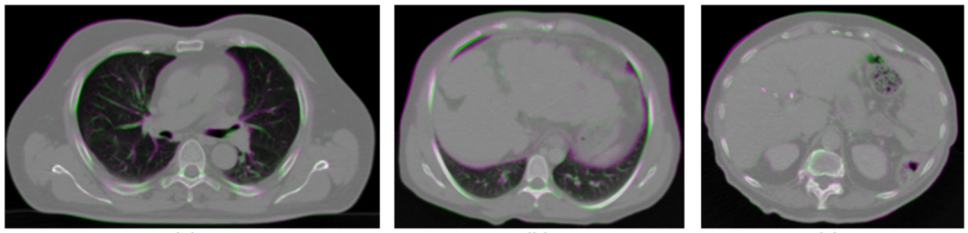

Figure 4. Demonstration of geometric distortion application with the overlay of undistorted CT (green) and distorted CT (purple) images, for (a) lung Patient 3 (b) liver Patient 3, and (c) pancreas Patient 2. Areas of agreement are depicted in gray scale.

values and smaller ranges in the abdominal sites compared to the lung. Specifically, the MAEs in the CTV had a median of 26.61 HU, 10.26 HU, and 17.15 HU in the lung, liver, and pancreas cases, respectively, with a range of 17.46–40.28 HU, 8.55–23.27 HU and 12.89–17.34 HU in the corresponding sites. MAE values higher than the median for the corresponding site were reported in the cases where the tumor was close to a rib (namely lung Patients 2, 3, 7, 8, and liver Patient 2).

3.2.2 Dosimetric impact of geometric distortions

3.2.2.1 Results in the target structure. The dosimetric impact of geometric distortions on the CTV DVH parameters was lower in the abdominal sites compared to the lung (Figure 5). Specifically, while in the abdominal sites ΔDHI medians had a maximum of 0.001, and the medians of the other DVH parameter differences were all below 0.10%, for the lung patients the medians of the $\Delta D_{2\%}$, $\Delta D_{98\%}$, and ΔD_{mean} parameters were 0.25%, 2.85%, 0.01%, respectively, and ΔDHI presented a median of 0.045. $\Delta D_{98\%}$ also exhibited the highest interquartile range in the lung cases (Figure 5(a)) with a range of 15.30% with respect to the prescribed dose. Indeed, in lung patients 1, 3 and 6, which presented an isolated tumor inside the lung parenchyma, $\Delta D_{98\%}$ was relatively higher varying between 15.90% and 21.50%, whereas, in the rest of the lung patients that presented a tumor close to soft tissue, $\Delta D_{98\%}$ was smaller reaching a maximum value of 5.60%. Findings from the quantification of the dosimetric impact of geometric distortions in the CTV structure DVH parameters for each patient are provided in Appendix B Table B1.

Figure 6 shows the dose distributions and DVH plots for four example patients: lung Patient 3 (a) and lung Patient 8 (b) (i.e. exemplary lung cases in which the tumor is isolated inside the lung parenchyma and close to the soft tissue, respectively), liver Patient 3 (c) and pancreas Patient 2 (d). The largest DVH deviation (with $\Delta D_{2\%} = 0.40\%$, $\Delta D_{98\%} = 21.50\%$, $\Delta D_{mean} = 3.25\%$, and $\Delta HI = 0.132$) was observed in lung Patient 3, in which the tumor was isolated in the lung parenchyma, whereas in the other exemplary patients the differences between undistorted and distorted CTV dose were comparably smaller, with $\Delta D_{98\%}$ reaching up to 0.40% and ΔDHI exhibiting a maximum value of 0.004.

According to the Wilcoxon matched-pairs signed-rank test at a 5% significance level, the dosimetric variation due to geometric distortions was found statistically significant in all of the target DVH parameters. Additionally, the Kruskal–Wallis test (alpha = 5%) confirmed the statistically significant difference among different anatomical sites for $\Delta D_{98\%}$ and ΔDHI. Indeed, as a result of the multiple comparison post-hoc test, the dosimetric change due to geometric distortions in the lung cases was found to come from a different distribution than the abdominal sites.

3.2.2.2 Results in OARs. Grouped average values were calculated in each OAR relying on the median across the whole patient group, as defined by the corresponding treatment site. The grouped average for ΔD_{mean} was 0.50%, 0.05%, and 1.18% in lung, liver and pancreas sites, respectively. Likewise, the grouped average for ΔD_{max} was 0.20%, 0.25% and 0.41% in the corresponding treatment sites. In the parallel OARs, the median of ΔD_{mean} reached a maximum value of 1.80% in the ipsilateral lung for the lung patient group, and 0.23% in the liver for the liver patient group. Accordingly, the dosimetric variations between undistorted and distorted dose distributions in the OARs were mainly quantified to be higher, compared to the grouped average, in the organs where the tumor was located. Above all, according to the Wilcoxon signed-rank test, the dosimetric impact of geometric distortions was found not statistically significant in OAR DVH parameters.

4 Discussion

The sensitivity of proton dose distributions to uncertainties and the resulting severe dose degradation when these uncertainties are not properly accounted for have been widely explored [2,38]. However, in the consideration of a clinical introduction of MRI-only proton therapy, studies in the literature mainly investigated the dosimetric effects of errors originating from synthetic CT generation methods [39–47], with no published papers, to the best of our knowledge, on the dosimetric effects of geometric distortions arising from MR imaging, especially for thoraco-abdominal tumors. In this study, a method has been introduced to quantify the dosimetric impact of system-dependent geometric distortions in

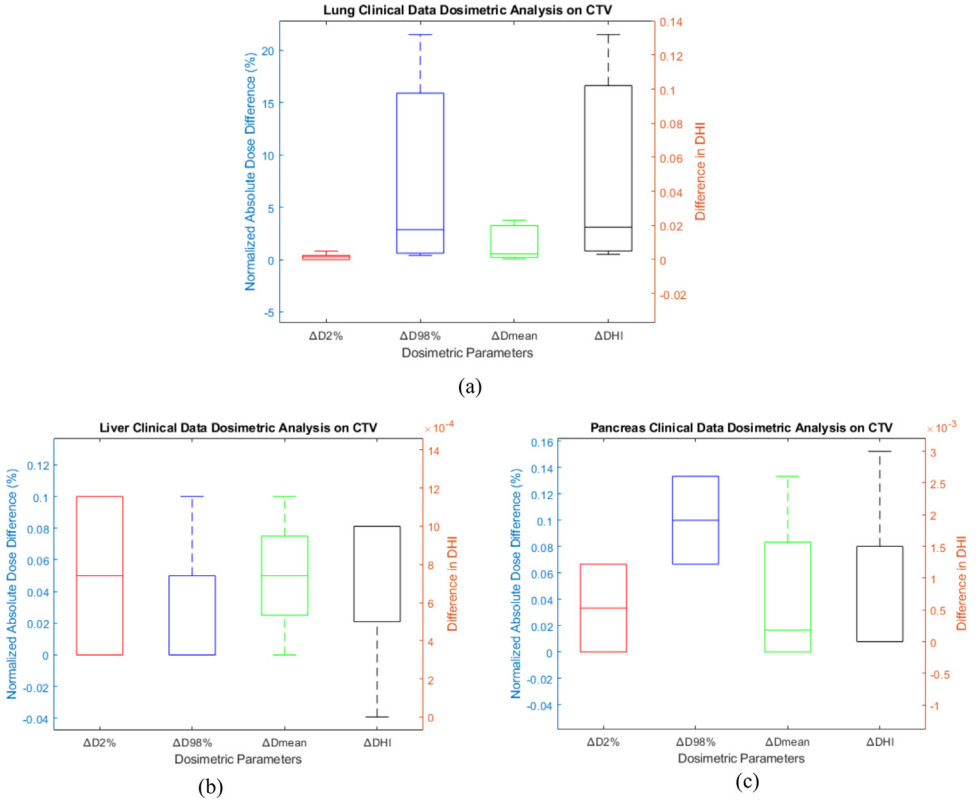

Figure 5. Box plots of the dosimetric changes in CTV DVH parameters for (a) lung, (b) liver and (c) pancreas clinical data in which $\Delta D_{2\%}$, $\Delta D_{98\%}$, $\Delta D_{mean\%}$ are shown in red, blue and green, respectively with their *y*-axis on the left and variation in dose homogeneity index (ΔDHI) is shown in black with its *y*-axis on the right.

an MRI-only proton therapy workflow for thoraco-abdominal sites, where organ motion requires special consideration for accurate planning. In the developed methodology, we mapped a distortion model, derived by phantom-based experimental quantification of MRI system-dependent geometric distortions, on 4D CT images. This allowed us to perform a pure analysis of the dosimetric effects of MRI spatial distortions, eliminating the inaccuracies arising from synthetic CT generation techniques. Such a setting is meant to provide an evaluation of the potential of treatment planning techniques in compensating for MRI spatial distortions. Our investigation does not therefore explore the complexity of MRI spatial distortion effects: specific studies are needed to address causes and sources of residual geometric distortion, and to provide optimization of the MR imaging sequence.

Our study considered dose delivery gated at exhale, relying on two beams in a single field uniform dose setting. The choice was motivated by the need to provide similar conditions for the applied beams and a homogeneous dose within the bsPTV. This allowed us to quantify the intrinsic effect of MRI distortions, independently of the applied dose modulation in a pure Intensity Modulated Proton Therapy (IMPT) setting. The use of more complex intensity modulation patterns deserves specific attention, as the location of MRI distortions with respect to the planned IMPT pattern is expected to introduce further variability in terms of dosimetric effects.

The methodology was first tested on a thoraco-abdominal digital phantom and the impact of geometric distortions quantified both in terms of voxel-level accuracy and dosimetric changes. Smaller MAEs were measured between the undistorted and the CTV volume in the abdominal phantoms compared to the lung phantom. Similarly, smaller dosimetric variations in the target structure were observed in the abdominal sites than in the thorax and dosimetric deviations in OARs were negligible.

As tissue inhomogeneities were not completely accounted for in the phantom simulations [48], we conducted a comprehensive study in 18 clinical thoraco-abdominal cancer patients. As a result of the application of geometric distortions, MAEs between the undistorted CT and the distorted CT in the whole body volume had a higher range in the lung site patient dataset compared to the abdominal sites. Moreover, MAEs between the undistorted and the distorted CTV volumes were quantified to have higher median value and variability in the lung cases than abdominal sites, which is attributable to the fact that higher density variations are present in the lung region around the tumor.

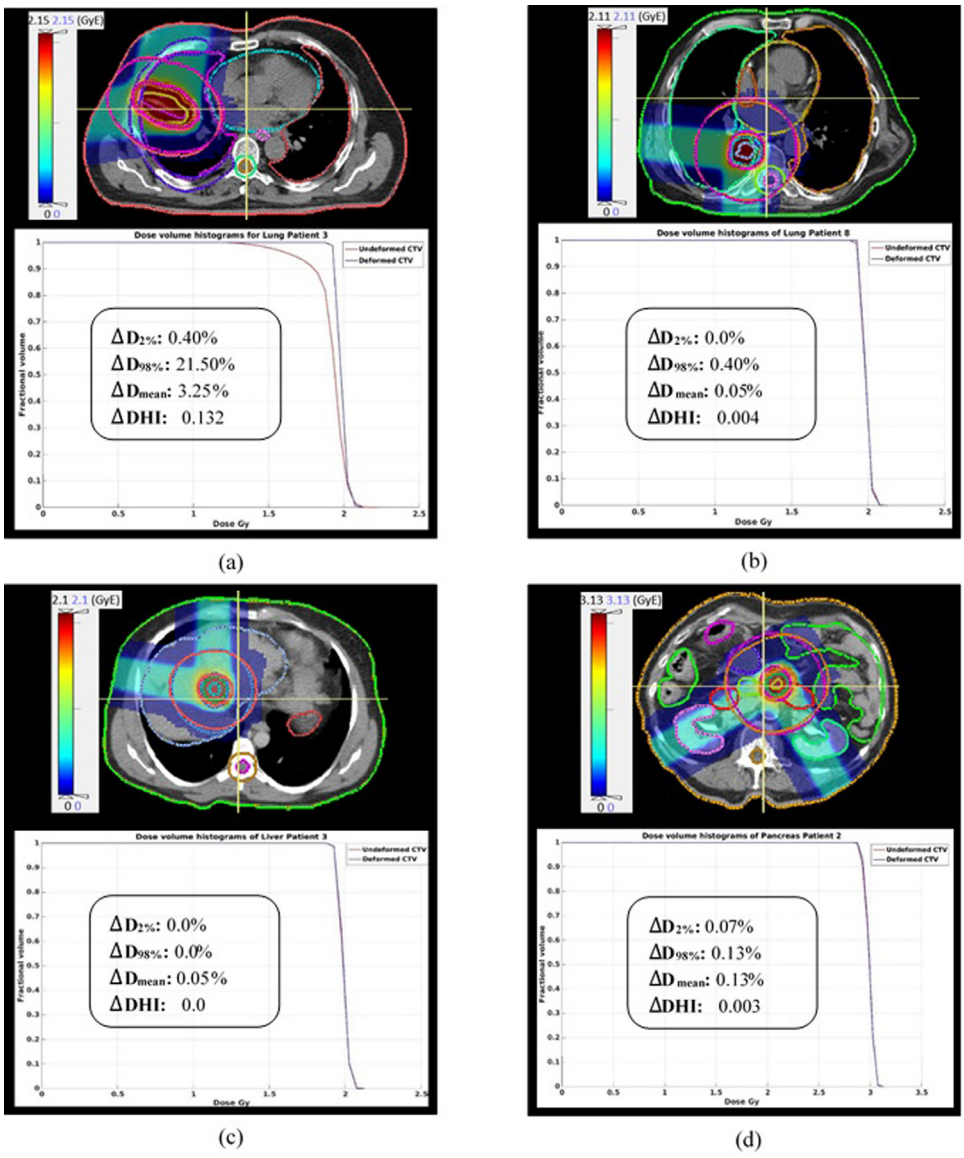

Figure 6. Dose distributions (on the top) for the distorted scan and DVH plots of the dose in CTV structure (on the bottom), in which the red curve belongs to the dose in the undistorted CT ($D_{undistorted}$) and the blue curve belongs to the dose in the distorted CT ($D_{distorted}$), for (a) lung Patient 3, where the tumor is isolated inside the lung parenchyma, (b) lung Patient 8, where tumor is close to soft tissue, (c) liver Patient 3, (d) pancreas Patient 2.

The target DVH parameters of the undistorted and distorted dose distributions were found to be statistically different at the 5% significance level in the clinical dataset, confirming that MRI geometric distortions introduce variations in the planned dose. Specifically, as a consequence of geometric distortions, higher dosimetric variations were quantified in the lung cases with $\Delta D_{98\%}$ (the DVH parameter exhibiting the highest variation) reaching 21.50% with respect to the prescribed dose and ΔDHI going up to 0.132, whereas lower dosimetric variations were quantified in the abdominal site with ΔDHI having a maximum value of 0.003 and the variation in terms of other DVH parameters staying below 0.13% with respect to the prescribed dose. As a result of the geometric distortion application, the variations of the induced dosimetric change among the lung and abdominal patient datasets comply with the MAE result patterns in the CTV volume for the corresponding sites.

The statistical analysis also highlighted that the dosimetric variations in terms of the $D_{98\%}$ and DHI parameters in the lung dataset came from a different distribution than the abdominal sites dataset (Kruskal–Wallis, alpha = 0.5). Different distribution among the datasets is attributable to the fact that tumors presented two different locations in the lung: isolated inside

the lung parenchyma or close to soft tissue, whereas it was always surrounded by soft tissues in the abdominal cases, as also demonstrated in the phantom cases. As such, while the dosimetric variation was higher for the lung cases with the tumor isolated inside the lung parenchyma away from the soft tissue ($\Delta D_{98\%}$ ranging between 15.90% and 21.50%), it was much smaller in the abdominal and lung cases where the tumor was within or close to the soft tissue ($\Delta D_{98\%} \leq 5.60\%$ in the relative lung cases and $\Delta D_{98\%} \leq 0.13\%$ in the abdominal cases). This is due to the fact that the beam configuration with the tumor isolated in the lung parenchyma is subject to high-density variations within the beam pathways due to the presence of dense ribs and air. In order to better investigate the impact of geometric distortions in presence of inhomogeneities, Monte Carlo (MC) optimization is worth to be investigated since it provides more robust and accurate planning and improves therapeutic benefit [59,60], especially in heterogeneous media [61].

Analyses on OARs were also conducted to evaluate potential over-dosage due to MR distortions. In this case, dosimetric differences due to geometric distortions were negligible and did not result significant.

In similar studies, Gustafsson et al. concluded that the mean dose deviation and dosimetric impact on radiotherapy structures due to system-dependent geometric distortions were insignificant for the prostate [33]. Conversely in Yan et al. distortions did not result in clinically meaningful dose deviations for 9 out of 14 patients, whereas in the rest of the 5 patients, including liver, prostate and head and neck cases, MRI distortions caused up to 3.6% loss of target coverage [35]. Although a direct comparison between our work and previous studies in the literature is not straightforward, since they are conducted in MRI-only conventional photon radiotherapy and evaluated different body regions with different parameters, our results were similar to the findings in the literature for abdominal sites [35]. Indeed, in the current study, dosimetric variations due to geometric distortions in target DVH parameters in the abdomen were quantified to be small and changes in OARs negligible.

The major limitation of our study is the limited patient dataset. The effect of geometric distortions on just three thorax cases where the tumor was isolated inside the lung parenchyma away from soft tissue, has been concluded to be appreciably higher than the other cases. Thus, an analysis on a larger patient cohort is required to safely integrate the MRI-only proton therapy workflow into the clinical practice for this anatomical site.

Even though the nonlinearity of the gradients is the dominant source of distortions [22], we may have underestimated the dose deviation caused by the geometric distortions in MRI, as the patient-dependent geometric distortions are not simulated in the current study. Conversely, the MRI sequence used in this study features a relatively low bandwidth (295 Hz/pixel), which is expected to lead to larger distortion compared to high bandwidth sequences, as typically applied for synthetic CT generation [62]. In our study, the dose distribution was not influenced by any errors that could originate from synthetic CT generation in an MRI-only workflow, for which the absolute maximum dose differences relative to CT were reported below 2% in earlier studies [39,63]. In order to consider all the real-life application aspects of MRI-only proton therapy and test the feasibility of this workflow in the clinical practice, further analyses would include the uncertainties introduced by patient-dependent geometric distortions and synthetic CT (sCT) generation. Synthetic CT generation methods based on deep learning [62,64,65,41] could potentially be employed to learn consistent differences in geometry between CT and MRI due to spatial distortion, thus providing a method for correction. This is expected to be feasible especially for deep learning based methods that do not assume perfect co-registration of CT and MRI for training, relying for example on cycle-consistent generative adversarial networks [41]. Additional investigations should be also focused on the reduction of the inaccuracies arising from HU to relative stopping power ratio conversion.

5 Conclusions

In this study, we aimed at quantifying the dosimetric impact of geometric distortions arising from MRI in an MRI-only proton therapy workflow in the thoraco-abdominal site. While the dosimetric impact of system-dependent geometric distortions in the target structure was higher for the lung cases, especially when the tumor was isolated inside the lung parenchyma away from the soft tissue, it was much smaller in the abdominal cases. In OARs, the dosimetric impact of geometric distortions was instead negligible. This study, therefore, suggests the potential applicability of MRI-only proton therapy, provided that analyses on a larger patient cohort are performed to conclude on the dosimetric impact of MRI distortions, especially when the tumor is isolated from the soft tissue inside the lung parenchyma.

Conflict of interest

The Department of Radiation Oncology of the University Hospital of LMU Munich has research agreements with Brainlab, Elekta and Viewray.

Acknowledgements

The authors acknowledge the help of Liheng Tian for the support in the use of the computational environment for radiological research CERR. MR acknowledges the support of the DFG Excellence Cluster MAP (Munich Center for Advanced Photonics).

Appendix A Displacement map generation

Geometric distortion artifacts in MR imaging were experimentally quantified using a self-designed distortion phantom with grid-like structure. MR images were made with a water-filled phantom (four physically aligned modules) using Magnetom AERA 1.5T Scanner from Siemens. The phantom was designed with Polymethyl methacrylate (PMMA) and had a total volume of $369 \times 300 \times 500\,mm^3$. Each phantom subunit housed 5 distortion grids with the edge dimensions of 5 mm for the rectangular grid bars and a spacing of 20 mm for the crossings. The phantom contained 3840 reference points distributed over 20 grids. A virtual model of the phantom was created in voxel space in accordance with the construction plan. Landmarks were added to the virtual model to be able to extract deformation information at the region of interest in the analysis of phantom images.

The phantom was verified relying on rigid image registration between the virtual model and a CT scan. CT-measurement of the phantom was performed using a Toshiba CT scanner (model: Aquilon LB) with a resolution of $1.074 \times 1.074 \times 1\,mm^3$ in order to verify that the digital model of distortion phantom accurately represented the real distortion grid. The RMSD of the phantom landmarks in the CT image and the virtual model after registration was found to be 1.00 mm for a registration based on the two central phantom modules, covering 250 mm in the superior-inferior direction.

After the completion of the CT-acquisition, MR imaging of the water-filled phantom was performed with a resolution of $1.172 \times 1.172 \times 5\,mm^3$. MR images were acquired with the following sGRE sequence: echo time 2.78 ms, repetition time 5.80 ms, flipping angle 8, bandwidth per pixel 295 Hz, with vendor-supplied 3D distortion correction. In order to extract the deformation field, non-rigid registration was calculated between the acquired MR images and the virtual phantom model. B-spline deformable image registration was implemented in Plastimatch (http://plastimatch.org/), relying on mutual information metric (Mattes) as a metric. The determined vector field (Figure A.1) was finally used to model the residual MRI distortion, i.e. the spatial distortion that is not adequately compensated by the applied distortion correction. For a more extensive description, the reader is referred to the analysis reported by Kroll et al [51].

Appendix B Dosimetric impact of geometric distortions in CTV in the patient cohort

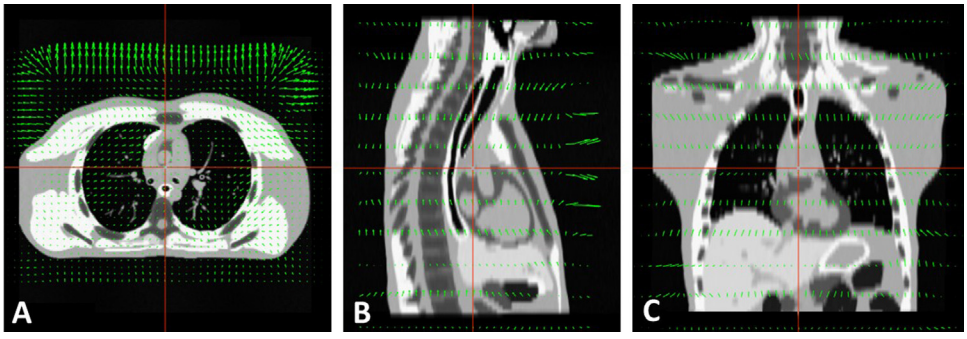

Figure A.1. Representation of the calculated 3D vector field representing MRI spatial distortions in axial (panel A), sagittal (panel B) and coronal (panel C) view. The vector field is overlaid to a digital phantom for better visualization.

Table B.1
Dosimetric change in CTV DVH parameters between undistorted and distorted dose distributions belonging to clinical cases (Dosimetric change in terms of $D_{2\%}$, $D_{98\%}$, D_{mean} parameters are normalized to the prescribed dose, which was 2 GyE in lung and liver cases and 3 GyE in pancreas case).

Anatomical site	Patient number	$D_{2\%}$ (%)	$D_{98\%}$ (%)	D_{mean} (%)	DHI
Lung	Patient 1	0.80	15.90	3.40	0.102
	Patient 2	0.40	5.60	0.85	0.027
	Patient 3	0.40	21.50	3.25	0.132
	Patient 4	0.80	4.0	0.70	0.026
	Patient 5	0.0	1.70	0.40	0.012
	Patient 6	0.30	17.60	3.75	0.129
	Patient 7	0.20	1.40	0.20	0.009
	Patient 8	0.0	0.40	0.05	0.004
	Patient 9	0.0	0.60	0.25	0.003

Table B.1 (*Continued*)

Anatomical site	Patient number	$D_{2\%}$ (%)	$D_{98\%}$ (%)	D_{mean} (%)	DHI
	Patient 10	0.0	0.60	0.10	0.005
Liver	Patient 1	0.10	0.10	0.0	0.001
	Patient 2	0.10	0.0	0.10	0.001
	Patient 3	0.0	0.0	0.05	0.0
	Patient 4	0.0	0.0	0.05	0.001
Pancreas	Patient 1	0.0	0.07	0.03	0.0
	Patient 2	0.07	0.13	0.13	0.003
	Patient 3	0.07	0.07	0.0	0.0
	Patient 4	0.0	0.13	0.0	0.0

References

[1] Durante M, Loeffler JS. Charged particles in radiation oncology. Nat Rev Clin Oncol 2010;7(1):37–43.
[2] Mohan R, Grosshans D. Proton therapy – present and future. Adv Drug Deliv Rev 2017;109:26–44.
[3] Paganetti H. Range uncertainties in proton therapy and the role of Monte Carlo simulations. Phys Med Biol 2012;57(11):99–117.
[4] Jaffray DA. Image-guided radiotherapy: from current concept to future perspectives. Nat Rev Clin Oncol 2012;9(12):688–99.
[5] Schneider U, Pedroni E, Lomax A. The calibration of CT Hounsfield units for radiotherapy treatment planning. Phys Med Biol 1996;41(1):111–24.
[6] Dirix P, Haustermans K, Vandecaveye V. The value of magnetic resonance imaging for radiotherapy planning. Semin Radiat Oncol 2014;24(3):151–9.
[7] Chandarana H, Wang H, Tijssen RHN, Das IJ. Emerging role of MRI in radiation therapy. J Magn Reson Imaging 2018;48(6):1468–78.
[8] Owrangi AM, Greer PB, Glide-Hurst CK. MRI-only treatment planning: benefits and challenges. Phys Med Biol 2018;63(5), 05TR01.
[9] Nyholm T, Nyberg M, Karlsson MG, Karlsson M. Systematisation of spatial uncertainties for comparison between a MR and a CT-based radiotherapy workflow for prostate treatments. Radiat Oncol 2009;4(54).
[10] Ulin K, Urie MM, Cherlow JM. Results of a multi-institutional benchmark test for cranial CT/MR image registration. Int J Radiat Oncol Biol Phys 2010;77(5):1584–9.
[11] Brunt JNH. Computed tomography-magnetic resonance image registration in radiotherapy treatment planning. Clin Oncol 2010;22(8):688–97.
[12] Karlsson M, Karlsson MG, Nyholm T, Amies C, Zackrisson B. Dedicated magnetic resonance imaging in the radiotherapy clinic. Int J Radiat Oncol Biol Phys 2009;74(2):644–51.
[13] Nyholm T, Jonsson J. Counterpoint: opportunities and challenges of a magnetic resonance imaging-only radiotherapy work flow. Semin Radiat Oncol 2014;24(3):175–80.
[14] Jonsson J, Nyholm T, Söderkvist K. The rationale for MR-only treatment planning for external radiotherapy. Clin Transl Radiat Oncol 2019;18:60–5.
[15] Edmund JM, Nyholm T. A review of substitute CT generation for MRI-only radiation therapy. Radiat Oncol 2017;12(1):12–28.
[16] Johnstone E, Wyatt JJ, Henry AM, Short SC, Sebag-Montefiore D, Murray L, et al. Systematic review of synthetic computed tomography generation methodologies for use in magnetic resonance imaging-only radiation therapy. Radiat Oncol Biol Phys 2018;100(1):199–217.
[17] Uh J, Merchant TE, Li Y, Li X, Hua C. MRI-based treatment planning with pseudo CT generated through atlas registration. Med Phys 2014;41(5):051711.
[18] Liu F, Yadav P, Baschnagel AM, McMillan AB. MR-based treatment planning in radiation therapy using a deep learning approach. J Appl Clin Med Phys 2019;20(3):105–14.
[19] Hsu HS, Cao Y, Huang K, Feng M, Balter JM. Investigation of a method for generating synthetic CT models from MRI scans of the head and neck for radiation therapy. Phys Med Biol 2013;58(23):8419–35.
[20] Kim J, Garbarino K, Schultz L, Levin K, Movsas B, Siddiqui MS, et al. Dosimetric evaluation of synthetic CT relative to bulk density assignment-based magnetic resonance-only approaches for prostate radiotherapy. Radiat Oncol 2015;10(239).
[21] Schmidt MA, Payne GS. Radiotherapy planning using MRI. Phys Med Biol 2015;60(22):323–61.
[22] Baldwin LN, Wachowicz K, Thomas SD, Rivest R, Fallone BG. Characterization, prediction, and correction of geometric distortion in 3 T MR images. Med Phys 2007;34(2):388–99.
[23] Wang D, Doddrell DM. A proposed scheme for comprehensive characterization of the measured geometric distortion in magnetic resonance imaging using a three-dimensional phantom. Med Phys 2004;31(8):2212–8.
[24] Fransson A, Adreo P, Pötter R. Aspects of MR image distortions in radiotherapy treatment planning. Strahlenther Onkol 2001:59–73.
[25] Torfeh T, Hammoud R, Perkins G, McGarry M, Aouadi S, Celik A, et al. Characterization of 3D geometric distortion of magnetic resonance imaging scanners commissioned for radiation therapy planning. Magn Reson Imaging 2016;34(5):645–53.
[26] Walker A, Liney G, Metcalfe P, Holloway L. MRI distortion: considerations for MRI based radiotherapy treatment planning. Australas Phys Eng Sci Med 2014;37(1):103–13.
[27] Weygand J, Fuller CD, Ibbott GS, Mohamed AS, Ding Y, Yang J, et al. Spatial precision in magnetic resonance imaging-guided radiation therapy: the role of geometric distortion. Int J Radiat Oncol Biol Phys 2016;95(4):1304–16.
[28] Wang D, Strugnell W, Cowin G, Doddrell DM, Slaughter R. Geometric distortion in clinical MRI systems Part I: evaluation using a 3D phantom. Magn Reson Imaging 2004;22(9):1211–21.
[29] Stanescu T, Jaffray D. Investigation of the 4D composite MR image distortion field associated with tumor motion for MR-guided radiotherapy. Med Phys 2016;43(3):1550–62.
[30] Huang KC, Cao Y, Baharom U, Balter JM. Phantom-based characterization of distortion on a magnetic resonance imaging simulator for radiation oncology. Phys Med Biol 2016;61(2):774–90.
[31] Torfeh T, Hammoud R, Mcgarry M, Al-Hammadi N, Perkins G. Development and validation of a novel large field of view phantom and a software module for the quality assurance of geometric distortion in magnetic resonance imaging. Magn Reson Imaging 2015;33(7):939–49.
[32] Karger CP, Höss A, Bendl R, Canda V, Schad L. Accuracy of device-specific 2D and 3D image distortion correction algorithms for magnetic resonance imaging of the head provided by a manufacturer. Phys Med Biol 2006;51(12):253–61.
[33] Gustafsson C, Nordström F, Persson E, Brynolfsson J, Olsson LE. Assessment of dosimetric impact of system-specific geometric distortion in an MRI only based radiotherapy workflow for prostate. Phys Med Biol 2017;62(8):2976–89.

[34] Adjeiwaah M, Bylund M, Lundman JA, Söderström K, Zackrisson B, Jonsson JH, et al. Dosimetric impact of MRI distortions: a study on head and neck cancers. Int J Radiat Oncol Biol Phys 2019;103(4):994–1003.
[35] Yan Y, Yang J, Beddar S, Ibbott G, Wen Z, Court LE, et al. A methodology to investigate the impact of image distortions on the radiation dose when using magnetic resonance images for planning. Phys Med Biol 2018;63(8):085005.
[36] Vyfhuis MAL, Onyeuku N, Diwanji T, Mossahebi S, Amin NP, Badiyan SN, et al. Advances in proton therapy in lung cancer. Ther Adv Respir Dis 2018;12:1–16.
[37] Raldow A, Lamb J, Hong T. Proton beam therapy for tumors of the upper abdomen. Br J Radiol 2019;92:20190226.
[38] Engelsman M, Schwarz M, Dong L. Physics controversies in proton therapy. Semin Radiat Oncol 2013;23(2):88–96.
[39] Koivula L, Wee L, Korhonen J. Feasibility of MRI-only treatment planning for proton therapy in brain and prostate cancers: dose calculation accuracy in substitute CT images. Med Phys 2016;43(8):4634–42.
[40] Liu Y, Lei Y, Wang Y, Shafai-Erfani G, Wang T, Tian S, et al. Evaluation of a deep learning-based pelvic synthetic CT generation technique for MRI-based prostate proton treatment planning. Phys Med Biol 2019;64(20):205022.
[41] Liu Y, Lei Y, Wang Y, Wang T, Ren L, Lin L, et al. MRI-based treatment planning for proton radiotherapy: dosimetric validation of a deep learning-based liver synthetic CT generation method. Phys Med Biol 2019;64(14):145015.
[42] Maspero M, van den Berg CAT, Landry G, Belka C, Parodi K, Seevinck PR, et al. Feasibility of MR-only proton dose calculations for prostate cancer radiotherapy using a commercial pseudo-CT generation method. Phys Med Biol 2017;62(24):9159–76.
[43] Pileggi G, Speier C, Sharp GC, Izquierdo Garcia D, Catana C, Pursley J, et al. Proton range shift analysis on brain pseudo-CT generated from T1 and T2 MR. Acta Oncol 2018;57(11):1521–31.
[44] Guerreiro F, Koivula L, Seravalli E, Janssens GO, Maduro JH, Brouwer CL, et al. Feasibility of MRI-only photon and proton dose calculations for pediatric patients with abdominal tumors. Phys Med Biol 2019;64(5):055010.
[45] Spadea MF, Pileggi G, Zaffino P, Salome P, Catana C, Izquierdo-Garcia D, et al. Deep Convolution Neural Network (DCNN) multiplane approach to synthetic CT generation from MR images – application in brain proton therapy. Int J Radiat Oncol Biol Phys 2019;105(3):495–503.
[46] Neppl S, Landry G, Kurz C, Hansen DC, Hoyle B, Stöcklein S, et al. Evaluation of proton and photon dose distributions recalculated on 2D and 3D Unet-generated pseudoCTs from T1-weighted MR head scans. Acta Oncol 2019;58(10):1429–34.
[47] Depauw N, Keyriläinen J, Suilamo S, Warner L, Bzdusek K, Olsen C, et al. MRI-based IMPT planning for prostate cancer. Radiat Oncol 2020;144:79–85.
[48] Paganelli C, Summers P, Gianoli C, Bellomi M, Baroni G, Riboldi M. A tool for validating MRI-guided strategies: a digital breathing CT/MRI phantom of the abdominal site. Med Biol Eng Comput 2017;55(11):2001–14.
[49] Deasy JO, Blanco AI, Clark VH. CERR: a computational environment for radiotherapy research. Med Phys 2003;30(5):979–85.
[50] Kroll C, Dietrich O, Bortfeldt J, Kamp F, Neppl S, Belka C, et al. Integration of spatial distortion effects in a 4D computational phantom for simulation studies in extra-cranial MRI-guided radiation therapy. Med Phys 2020 [Epub ahead of print].
[51] Schell S, Wilkens JJ. Advanced treatment planning methods for efficient radiation therapy with laser accelerated proton and ion beams. Med Phys 2010;37(10):5330–40.
[52] Chang JY, Zhang X, Knopf A, Li H, Mori S, Dong L, et al. Consensus guidelines for implementing pencil-beam scanning proton therapy for thoracic malignancies on behalf of the PTCOG thoracic and lymphoma subcommittee. Int J Radiat Oncol Biol Phys 2017;99(1):41–50.
[53] Kang Y, Zhang X, Chang JY, Wang H, Wei X, Liao Z, et al. 4D Proton treatment planning strategy for mobile lung tumors. Int J Radiat Oncol Biol Phys 2007;67(3):906–14.
[54] Hong TS, DeLaney TF, Mamon HJ, Willett CG, Yeap BY, Niemierko A, et al. A prospective feasibility study of respiratory gated proton beam therapy for liver tumors. Pract Radiat Oncol 2014;4(5):316–22.
[55] Jethwa KR, Tryggestad EJ, Whitaker TJ, Giffey BT, Kazemba BD, Neben-Wittich MA, et al. Initial experience with intensity modulated proton therapy for intact, clinically localized pancreas cancer: clinical implementation, dosimetric analysis, acute treatment-related adverse events and patient-reported outcomes. Adv Radiat Oncol 2018;3(3):314–21.
[56] Moyers MF, Miller DW, Bush DA, Slater JD. Methodologies and tools for proton beam design for lung tumors. Int J Radiat Oncol Biol Phys 2001;49(5):1429–38.
[57] Engelsman M, Kooy HM. Target volume dose considerations in proton beam treatment planning for lung tumors. Med Phys 2005;32(12):3549–57.
[58] Kataria T, Sharma K, Subramani V, Karrthick KP, Bisht SS. Homogeneity index: an objective tool for assessment of conformal radiation treatments. J Med Phys 2012;37(4):207–13.
[59] Yepes P, Adair A, Grosshans D, Mirkovic D, Poenisch F, Titt U, et al. Comparison of Monte Carlo and analytical dose computations for intensity modulated proton therapy. Phys Med Biol 2018;63(4):045003.
[60] Sasidharan BK, Aljabab S, Saini J, Wong T, Laramore G, Liao J, et al. Clinical Monte Carlo versus pencil beam treatment planning in nasopharyngeal patients receiving IMPT. Int J Part Ther 2019;5(4):32–40.
[61] Maes D, Saini J, Zeng J, Rengan R, Wong T, Bowen SR. Advanced proton beam dosimetry part II: Monte Carlo vs. pencil beam-based planning for lung cancer. Trans Lung Cancer Res 2018;7(2):114–21.
[62] Maspero M, Savenije MHF, Dinkla AM, Seevinck PR, Intven MPW, Jurgenliemk-Schulz IM, et al. Dose evaluation of fast synthetic-CT generation using a generative adversarial network for general pelvis MR-only radiotherapy. Phys Med Biol 2018;63(18):185001.
[63] Koivula L, Wee L, Korhonen J. Proton therapy treatment planning with MRI only: dose calculation accuracy in MRI-derived substitute computed tomography images for brain tumor and prostate cancer treatments. Int J Radiat Oncol Biol Phys 2016;96(2):E623.
[64] Fetty L, Löfstedt T, Heilemann G, Furtado H, Nesvacil N, Nyholm T, et al. Investigating conditional GAN performance with different generator architectures, an ensemble model, and different MR scanners for MR-sCT conversion. Phys Med Biol 2020;65(10):105004.
[65] Liu L, Johansson A, Cao Y, Dow J, Lawrence TS, Balter JM. Abdominal synthetic CT generation from MR Dixon images using a U-net trained with 'semi-synthetic' CT data. Phys Med Biol 2020;65(12):125001.